Geophysical Research Letters

RESEARCH LETTER
10.1029/2019GL085344

Impacts of Water Vapor on Saharan Air Layer Radiative Heating

Manuel Gutleben[1], Silke Groß[1], Martin Wirth[1], Claudia Emde[2], and Bernhard Mayer[2]

[1]Institute of Atmospheric Physics, German Aerospace Centre (DLR), Weßling, Germany, [2]Meteorological Institute, Ludwig-Maximilians-University (LMU), Munich, Germany

Key Points:
- Airborne lidar measurements indicate enhanced water vapor concentrations in Saharan air layers compared to the surrounding atmosphere
- Saharan air layer water vapor strongly modifies atmospheric radiative heating rate profiles
- Water vapor promotes mixing inside the dust layers and helps to maintain their bounding inversions

Correspondence to:
M. Gutleben,
manuel.gutleben@dlr.de

Citation:
Gutleben, M., Groß, S., Wirth, M., Emde, C., & Mayer, B. (2019). Impacts of water vapor on Saharan air layer radiative heating. *Geophysical Research Letters*, *46*, 14,854–14,862. https://doi.org/10.1029/2019GL085344

Received 9 SEP 2019
Accepted 29 NOV 2019
Accepted article online 4 DEC 2019
Published online 23 DEC 2019

Abstract Airborne lidar observations of long-range transported Saharan air layers in the western North Atlantic trades indicate increased amounts of water vapor within the dust layers compared to the surrounding dry free atmosphere. This study investigates the impact of such enhanced water vapor concentrations on radiative heating. Therefore, spatially high resolved airborne high spectral resolution and differential absorption lidar measurements are used for the parametrization of aerosol optical properties and water vapor concentrations in radiative transfer calculations. Heating rates that are calculated under consideration of the measured water vapor distribution strongly differ from heating rates that are derived under assumption of an atmospheric reference water vapor profile which is steadily decreasing with altitude. Results highlight that water vapor represents a major radiative driver for dust layer vertical mixing and the maintenance of bounding inversions at the top and bottom of the dust layer.

Plain Language Summary Dust particles are frequently mobilized in the Saharan desert and cross the subtropical North Atlantic Ocean in an elevated atmospheric dust layer, which is termed the Saharan air layer. Airborne remote sensing measurements that were conducted near the Caribbean islands indicate increased water vapor concentrations inside such dust layers compared to the surrounding dust-free atmosphere. In this work the radiative effect of water vapor in dust layers is investigated for the first time using measurements by an airborne lidar instrument together with a radiative transfer model. It is demonstrated that atmospheric heating due to water vapor is influencing the stability of the atmosphere and is a major driver for the maintenance of thermodynamic structure of the the dust layers.

1. Introduction

Aeolian mineral dust is one of the major contributors to the global tropospheric aerosol load (d'Almeida et al., 1991; Kinne et al., 2006) and is also known to play a key role in the Earth's climate system (Satheesh and Moorthy, 2005). It impacts the atmosphere's radiation budget by scattering, absorbing, and emitting radiation and by acting as nucleus for ice and water droplet formation (Boose et al., 2016; Karydis et al., 2011).

Earth's greatest source region of mineral dust is the Saharan desert. Every year 0.2 to 1.0 Gt of Saharan mineral dust particles gets mobilized over the Saharan desert (Huneeus et al., 2011). Approximately 25 % thereof are transported westward over the North Atlantic Ocean embedded in an elevated layer, the so-called Saharan air layer (SAL; Carlson and Prospero, 1972; d'Almeida et al., 1991). During the peak season of transatlantic dust transport from June to August (Moulin et al., 1997) the SAL is frequently advected thousands of kilometers toward the Caribbean islands. Measurements inside long-range transported SALs, which were conducted within the framework of the SALTRACE field campaign (Saharan Aerosol Long-range Transport and Aerosol-Cloud-Interaction Experiment; Weinzierl et al., 2017), did not indicate significant changes of dust optical and microphysical properties compared to dust near source regions (Groß et al., 2015). Even giant particles were still found in long-range transported dust layers after several days (Weinzierl et al., 2017). Gasteiger et al. (2017) suggested that vertical mixing processes may cause this almost undisturbed transport across the Atlantic Ocean and assumed that radiative effects may be the main driver for SAL mixing. However, studies with focus on Saharan dust radiative effects and heating rates rather concentrated on source regions and areas at the origin of dust transport (Kanitz et al., 2013; Li et al., 2004; Mallet et al., 2009; Zhu et al., 2007) and profound understanding on radiative transfer in long-range transported

SALs is missing so far. Furthermore, studies that consider measured water vapor profiles in the SAL have not been conducted.

In general, model simulations suggest that after long-range transport calculations of SAL heating rates are very sensitive to the water vapor profile (Wong et al., 2009). Especially in long-range transported SAL regimes a correct parametrization of the water vapor profile in radiative transfer models would therefore be of high importance, since SALs were found to take up moisture over the Saharan desert (Marsham et al., 2008), which often gets further transported across the Atlantic Ocean (Jung et al., 2013). However, studies focusing on radiative heating rate calculations, which employ simultaneous measurements of water vapor and aerosol profiles, have not yet been performed. Prior studies lack water vapor measurements and had to take its vertical distribution from model simulations or standard atmospheric profiles.

In this study simultaneous measurements of water vapor and aerosol optical properties from vertically highly resolved lidar measurements are used for the first time to investigate radiative heating rates in long-range transported SALs. The analysis concentrates on the effect of water vapor in heating rate calculations and compares the results to calculations, which use an assumed climatological reference profile that is continuously decreasing with altitude for the parametrization of the atmospheric water vapor distribution.

2. Methods and Instrumentation

In August 2016 airborne lidar measurements of transported SALs were conducted out of Barbados within the framework of the NARVAL-II field campaign (Next-generation Aircraft Remote-sensing for Validation Studies-II; Stevens et al., 2019). The German research aircraft HALO (High Altitude and Long Range; Krautstrunk and Giez, 2012) served as an airborne observatory for 10 research flights. During NARVAL-II the aircraft was equipped with a remote sensing payload including the WALES lidar instrument (Water Vapor Lidar Experiment in Space; Wirth et al., 2009). It served as a key instrument for vertical aerosol and water vapor profiling, since it combines water vapor Differential Absorption (DIAL) and depolarization sensitive High Spectral Resolution Lidar technique (HSRL; Esselborn et al., 2008). WALES enables measurements of water vapor mass mixing ratios (r_m) as well as particle extinction coefficients ($\alpha_{p(532)}$), backscatter ratios (R_{532}) and particle linear depolarization ratios ($\delta_{p(532)}$) at 532 nm from ground level to aircraft altitude. Due to the high pulse repetition rate of the instrument, water vapor measurements with relative uncertainties of less than 5% are achieved (Kiemle et al., 2008). The vertical resolution amounts to 15 and 150 m for HSRL and water vapor DIAL measurements. Along the flight track data sets are temporally averaged to 16 s (DIAL) and 1 s (HSRL) for signal-noise reduction. This results in horizontal resolutions of 3.2 km (DIAL) and 0.2 km (HSRL) at a typical aircraft speed of 200 m/s.

For radiative transfer calculations, WALES lidar measurements are related to aerosol optical properties. For this reason, a stepwise "particle extinction to mass concentration" conversion at 532 nm is performed. First, thresholds in $\delta_{p(532)}$ as discussed by Groß et al. (2011) and Burton et al. (2012) are used to locate regions of marine aerosol, mineral dust, and marine/mineral dust aerosol mixtures in vertical lidar profiles. Second, the contribution of mineral dust and marine aerosol to the total aerosol extinction coefficient in mixed aerosol regimes is determined analogously to the method described by Tesche et al. (2009) and Groß et al. (2011). In a third step, conversion coefficients are used to calculate the aerosol mass concentration in the three regimes from mineral dust and marine aerosol extinction coefficients (Groß et al., 2016; Mamouri and Ansmann, 2016). As Saharan dust particle optical properties are known not to alter in the course of long-range transport (Weinzierl et al., 2017), derived aerosol mass concentrations are in a last step related to the latest OPAC Version 4.0 (Optical Properties of Aerosols and Clouds; Koepke et al., 2015) aerosol optical properties for mineral dust and marine aerosol (i.e., scattering phase function, single scattering albedo, and asymmetry parameter). Mineral dust optical properties are hereby calculated employing T-matrix theory (Waterman, 1971) to account for highly irregular dust particle shapes.

Radiative heating rates are finally inferred utilizing profiles of aerosol optical properties and water vapor mass mixing ratios for calculations with the radiative transfer model libRadtran (Library for Radiative Transfer; Emde et al., 2016; Mayer and Kylling, 2005). The radiative transfer equation is hereby solved in both the shortwave (SW; 0.12–4.00 μm) and longwave (LW; 2.5–100.0 μm) spectral range using the discrete ordinate solver DISORT (Stamnes et al., 1988) with an improved intensity correction (Buras et al., 2011) and 16 streams. Molecular absorption is parameterized employing k-distribution methods in the SW (Kato et al.,

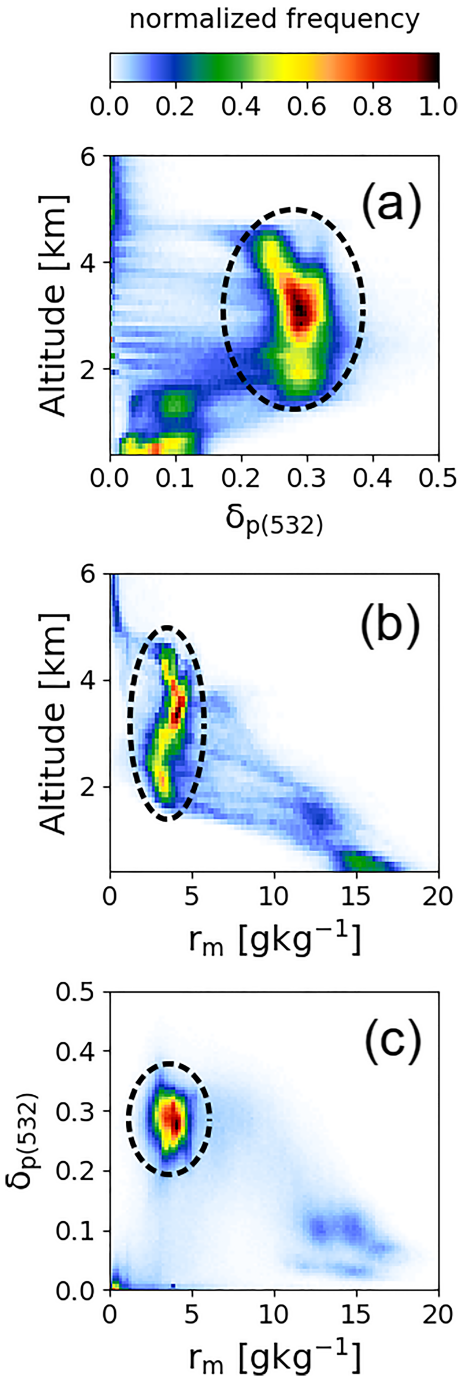

Figure 1. The 2-D histograms showing the distribution of measured 532-nm depolarization ratios ($\delta_{p(532)}$, (a)) and water vapor mass mixing ratios (r_m, (b)) as a function of altitude during the four NARVAL-II research flights leading over elevated Saharan dust layers. (c) The 2-D histogram of r_m as a function of $\delta_{p(532)}$ during the four NARVAL-II research flights leading over elevated Saharan dust layers. The distributions are normed to the maximum bin count in each individual histogram. Dashed regions indicate signatures of Saharan air layers.

1999) and LW (Fu and Liou, 1992). Reference profiles described in Anderson et al. (1986) are used to characterize tropical trace gas concentrations, for example, the ozone distribution. Uncertainties regarding surface albedo are minimized using the model-embedded bidirectional reflectance distribution function (BRDF; Bellouin et al., 2004; Cox and Munk, 1954), which relates 10-m wind speed (u_{10}) to sea swell and thus sea surface albedo. To obtain best results,u_{10} wind speed inferred from dropsonde measurements serves as BRDF input. Additionally, the temperature profile from dropsonde measurements is used for the characterization of the model temperature. Sea surface temperatures during NARVAL-II are taken from Moderate-resolution Imaging Spectroradiometer (MODIS) measurements, which were found to take constant values of 302 K in the measurement region.

3. Results

3.1. Enhanced Concentrations of Water Vapor in SALs

Within the framework of NARVAL-II a total of four research flights (16 flight hours) were designed to lead over regions comprising long-range transported SALs. During all of those flights, WALES lidar measurements showed enhanced concentrations of water vapor inside SALs compared to the surrounding dry free troposphere. Profiles of $\delta_{p(532)}$ can be used to identify SALs, since Saharan dust is characterized by values of $\delta_{p(532)}$ around 0.3 (Groß et al., 2015). The distribution of $\delta_{p(532)}$ measured during all research flights in dust-laden regions (Figure 1a) shows that all observed SALs have been elevated in the height interval from 2 to 5 km. In contrast, small values of $\delta_{p(532)}$ are found in the marine boundary layer (MBL), which always ranged up to about 1.5-km altitude. The measured water vapor distribution (Figure 1b) indicates that the height interval from 2 to 5 km is additionally characterized by water vapor mixing ratios around 4 g/kg. This is also highlighted by the joint distribution of both variables (Figure 1c). It clearly indicates the correlation of enhanced water vapor mixing ratios of 4 g/kg and typical values of $\delta_{p(532)}$ for Saharan dust layers around 0.3.

Figure 2 presents measurements of such a moist, elevated, and long-range transported SAL on 19 August 2016, as a representative case study for the characteristics of long-range transported SALs and their effects. The 2-D cross section of R_{532} (Figure 2c) measured during this research flight indicates the SAL ranging from 2.5- to 5.0-km altitude. In those altitudes $\delta_{p(532)}$ takes typical values for mineral dust around 0.3 (Figure 2b), R_{532} shows values around 3.0 (Figure 2d), and the layer aerosol optical depth at 532 nm is approximately 0.3 (not shown).

Homogeneously distributed water vapor mass mixing ratios around 4 g/kg are observed in SAL altitudes (Figure 2a). The profile of r_m follows the SAL signature in the R_{532} profile and indicates that the SAL represents a relatively moist layer compared to the surrounding dry free trade wind troposphere where r_m is smaller than 1 g/kg. Only the MBL which extends from the ocean surface to approximately 1.5-km altitude shows higher water vapor mixing ratios of up to 15 g/kg.

WALES lidar cross sections also show that the SAL is well separated from the MBL by an almost aerosol-free airmass. $\delta_{p(532)}$ inside the MBL takes values around 0.2—an indicator for a mixed MBL containing settling mineral dust and marine aerosol particles at lowest atmospheric levels. This is also reflected in derived profiles of marine and mineral dust aerosol mass concentration c_m. Mineral dust mass concentrations are highest at the center of the SAL reaching values of up to 120 g/m^3. At lower atmospheric levels the aerosol

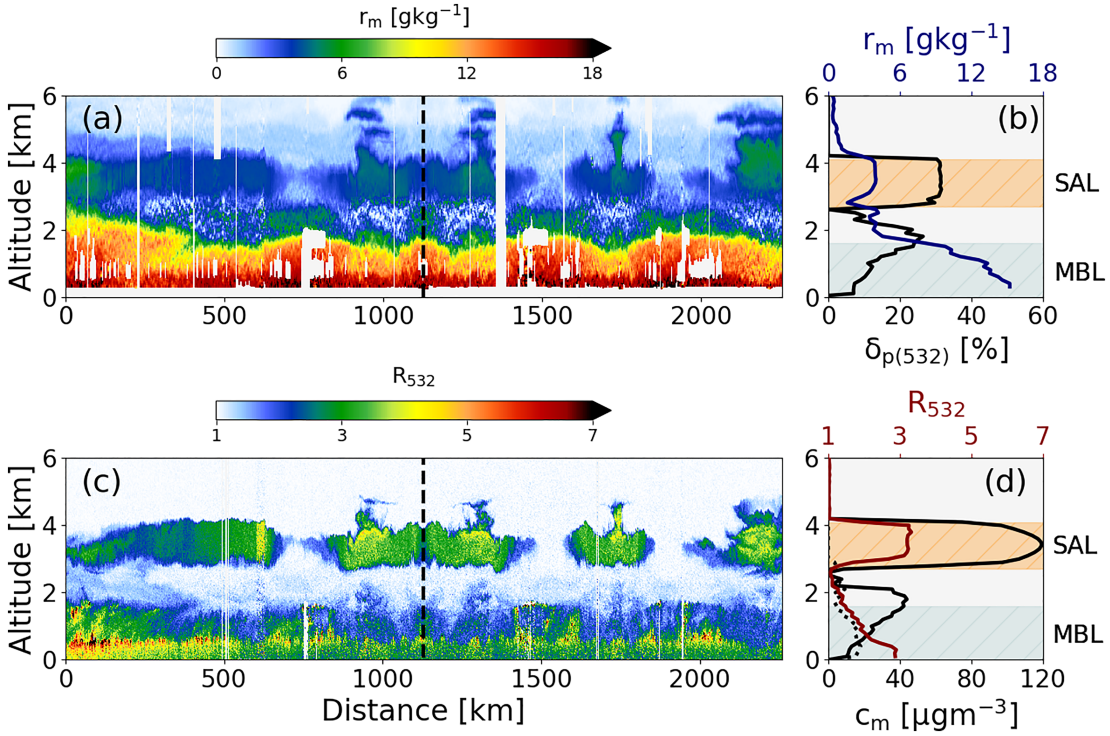

Figure 2. (a) The cross section of water vapor mass mixing ratio r_m measured during the research flight on 19 August 2016. (b) The vertical profiles of water vapor mass mixing ratio r_m and particle linear depolarization ratio $\delta_{p(532)}$ at the indicated measurement location (dashed lines in a and c). Hatched areas indicate the Saharan air layer (SAL, orange) and the marine boundary layer (MBL, light green). (c) The cross section of lidar backscatter ratio R_{532} measured during the research flight on 19 August 2016. (d) The vertical profiles of R_{532} as well as derived mineral dust (solid) and marine aerosol mass concentrations (dashed) at the indicated measurement location (dashed lines in a and c).

profile is composed of an aerosol mixture consisting of dust aerosol ($c_m > 40\,g/m^3$) and marine aerosol ($c_m > 20\,g/m^3$) with highest concentrations of marine aerosol at near-surface levels. In SAL altitudes no marine aerosol is detected anymore.

Calculated Hybrid Single Particle Lagrangian Intergated Trajectory Model (HYSPLIT; Stein et al., 2015) backward trajectories with National Centers for Environmental Prediction Global Data Assimilation System (NCEP GDAS) input data indicate that the SAL traveled for about 10 days from the Saharan desert to the measurement location in the southern part of the flight track (Figure 3a). The center of the SAL descended by more than 3 km (from 7 to 3.5 km). A huge dust-outbreak off-coast Senegal is also seen in MODIS and CALIOP (Cloud-Aerosol Lidar with Orthogonal Polarization) satellite observations on 15 August 2016 (Figures 3b and 3d). Enhanced backscatter in CALIOP lidar measurements indicate that the SAL was located in altitudes ranging from approximately 2- to 5-km altitude during the outbreak. Operationally launched radiosonde measurements on the same day over the city of Dakar (Senegal; Figure 3c) reveal that the SAL already showed enhanced r_m of up to 7 g/kg at the origin of its long-range transport.

3.2. SAL Heating Rates

Effects of the water vapor distribution in calculations are quantified by calculating diurnal (24 hr) averaged heating rate profiles for the lidar profiles shown in Figures 2b and 2d that are derived considering the measured mean profile of r_m ("lidar case") and by comparing them to a "reference case" for which a tropical standard water vapor profile—which describes the annual average water vapor profile at 15°N and is steadily decreasing with height (Anderson et al., 1986)—is used for simulations (Figure 4). Moreover, the aerosol contribution to the total radiative heating rate in the "lidar case" is calculated as the difference of heating rates that consider mineral dust aerosol and heating rates calculated without mineral dust aerosol in the model-atmosphere ("dust contribution").

Large differences are identified by comparing those three scenarios. SW heating rates of the "reference case" (Figure 4b) take values around 1 K/day throughout the whole profile and only show a slight increase in SAL altitudes (+0.2 K/day). With the water vapor distribution in the "reference case" being steadily decreasing

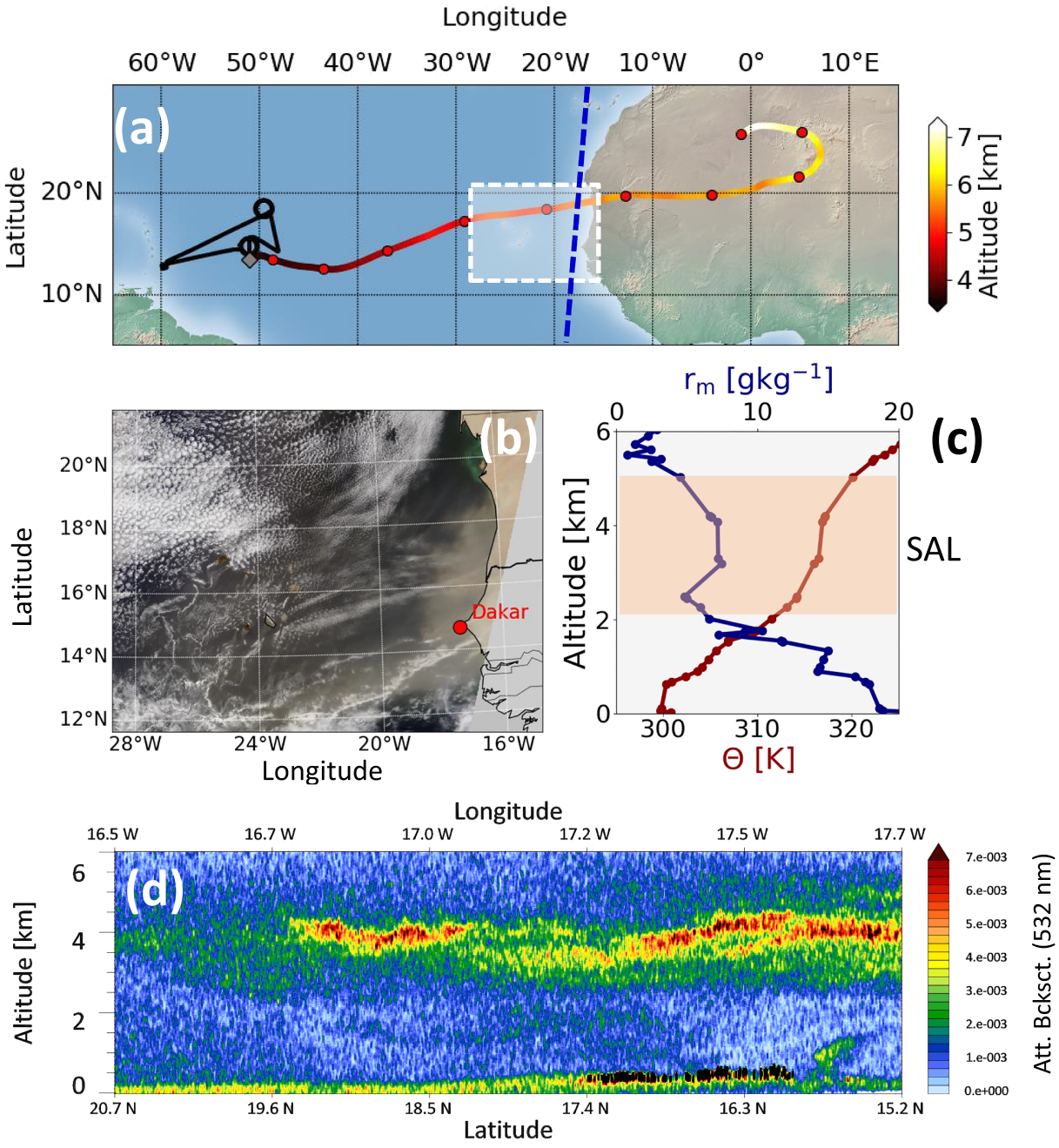

Figure 3. (a) The 10-day backward trajectory with the starting point being located inside the observed Saharan air layer (SAL; 19 August 2016 at 14:30 UTC; 14°N; 51.5°W; 3.5-km altitude). Colors mark the altitude of the trajectory. The black line in (a) marks the HALO research flight track on 19 August 2016. The white box in (a) indicates the field of view of the MODIS (Moderate-resolution Imaging Spectroradiometer) real color image illustrated in (b), which shows the dust outbreak region over Dakar (image taken on 15 August 2016 at 12:25 UTC). The dashed blue line in (a) marks the ground track of the smoothed 2-D CALIOP (Cloud-Aerosol LIdar with Orthogonal Polarization) 532-nm attenuated backscatter cross section of the observed SAL on 15 August 2016 around 03:00 UTC that is shown in (d). (c) Profiles of potential temperature Θ and water vapor mass mixing ratio r_m from radiosonde measurements over Dakar on 15 August 2016 at 12:00 UTC. The orange-colored region marks the observed SAL.

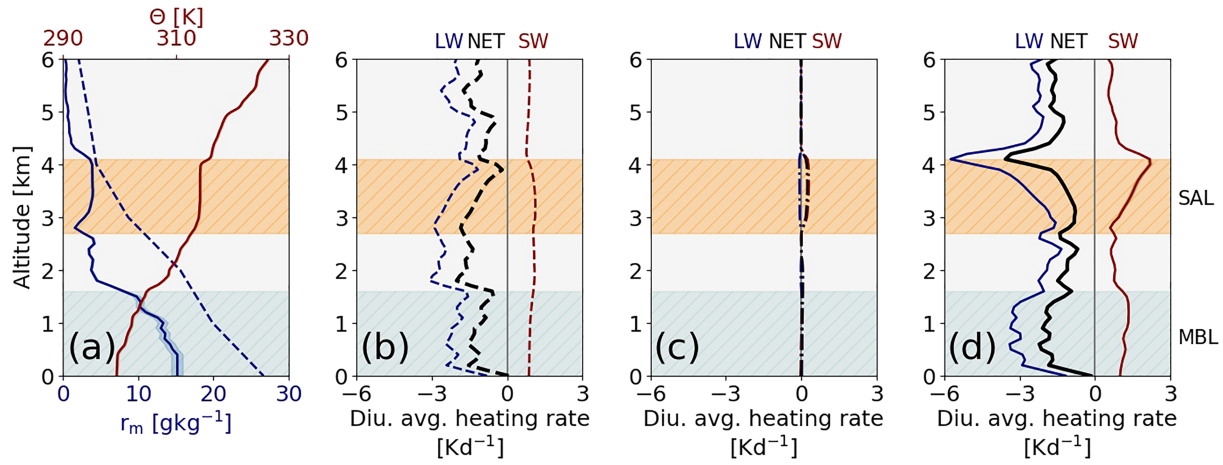

Figure 4. (a) Profiles of measured potential temperature Θ (red—dropsonde) and water vapor mass mixing ratio r_m (blue solid—DIAL) measured at 14°N, 51.5°W together with the reference profile of r_m for tropics as described in Anderson et al. (1986) (blue dashed). (b) Longwave (LW), shortwave (SW), and net heating rate profiles calculated considering the lidar-derived aerosol mass concentrations (c_m), the reference profile of r_m, and Θ from the dropsonde measurements. (c) Mineral dust aerosol contribution to the LW, SW, and net heating rate profiles (difference between calculated heating rates that consider c_m and heating rates that are calculated under assumption of aerosol free conditions). (d) LW, SW, and net heating rate profiles calculated considering profiles of r_m and c_m from the lidar measurements as well as Θ from the dropsonde measurements. Hatched areas mark the position of the observed Saharan air layer (SAL, orange) and the marine boundary layer (MBL, light green).

with altitude and not showing any strong gradients, SW heating rates also remain relatively unchanged with altitude. The slight increase in SAL altitudes is related to mineral dust absorption, since for the "dust contribution" scenario SW heating rates are also increased (+0.2 K/day; Figure 4c). A differently structured SW profile is derived for the "lidar-case" (Figure 4d). For this scenario SW heating rates in MBL altitudes fluctuate around +1.6 K/day and decrease to +1.0 K/day toward the bottom of the SAL. The most prominent feature, however, is the increase of SW heating with altitude in the SAL, which is peaking at the top of the SAL with +2.2 K/day. Maximum SW absorption takes place at the top of the dust layer, where a sudden increase in r_m toward lower atmospheric layers is located and most of the incident light in water vapor absorption bands gets absorbed. Another strong gradient in r_m is located at the top of the MBL. As a result SW heating rates also show a local maximum in these altitudes.

Derived LW and net heating rate profiles for the three scenarios differ as well. Calculations for the "dust contribution" in the LW spectral range reveal that mineral dust aerosol is associated with just a small cooling effect (−0.1 K/day). In contrast, inferred heating rates for the "reference case" indicate strong LW and net radiative cooling inside the MBL (LW: −2.7 K/day, net: −1.5 K/day). A sharp gradient toward even greater cooling rates of −3.0 K/day, which is likely associated with the decrease of potential temperature Θ in these altitudes, tops the MBL. Inside the SAL LW cooling weakenes with altitude (SAL bottom: −3.0 K/day; SAL top: −2.0 K/day). This decrease is also seen in SAL net radiative cooling (SAL bottom: −2.0 K/d; SAL top: −1.0 K/d), since LW cooling dominates SW heating in the whole profile. The LW heating rate profile also controls the shape of the net heating rate profile inside the MBL where cooling rates around −1.5 K/day are found. Overall, the shapes and features of LW and net heating rate profiles for the "reference case" are primarily defined by the used temperature profile in radiative transfer calculations. The structure of the calculated LW and net heating rate profile for the "lidar case" is substantially different. While profiles inside the MBL are quantitatively similar to the "reference case" (LW: −3.3 K/day, net: −2.3 K/day), profiles in the SAL region show different behaviors. In contrast to the "reference case," SAL LW and net radiative cooling increase with altitude both showing maximum cooling rates at the top of the SAL (LW: −6.0 K/day, net: −3.8 K/day). Largest LW cooling due to emission of radiation toward space is strongest at the top of the SAL, because no LW heating due to atmospheric counterradiation from higher atmospheric levels takes place there.

Overall, not dust particle but water vapor radiative effects are the strongest contributor to atmospheric heating rates in long-range transported SALs during NARVAL-II. Differences between the "reference case" and the "lidar case" highlight the strong effect of water vapor inside the SAL on the modification of the SW

and LW atmospheric radiative heating profile. Strongest effects are thereby observed at strongest negative gradients in r_m.

4. Discussion and Conclusion

All measurements above long-range transported SALs indicated enhanced water vapor mixing ratios of 4 g/kg inside the dust layers compared to the surrounding air masses. These findings fit well to former observations of water vapor mixing ratios in elevated SALs.

Kanitz et al. (2014) derived water vapor mass mixing ratios of 4–5 g/kg inside SALs form shipborne Raman lidar and microwave radiometer measurements over the Atlantic Ocean. Jung et al. (2013) deduced similar SAL mixing ratios from radiosonde measurements at the coast of Africa. They also conducted radiosonde observations over Barbados, which showed a further enhancement of 2 g/kg inside the SAL. They suggested that this enhancement may be caused by entrainment during long-range transport. Marsham et al. (2008) show that air masses over the Saharan desert are already characterized by slightly enhanced water vapor mixing ratios. Shown radiosonde measurements during NARVAL-II over the city of Dakar (section 3.1 and Figure 3) also indicated enhanced SAL water vapor. From those measurements it is suggested that water vapor uptake during activation processes might also be an important factor for SAL moistening.

Water vapor associated with transported SALs was found to have a large impact on SAL radiative heating. Not only it is the strongest contributor to calculated heating rate profiles, but also it significantly changes their vertical structure. Inside the SAL the net radiative heating rate is entirely negative and the cooling increases with height. Lilly (1968) showed that such an increase with altitude tends to decrease static stability and to promote vertical mixing. This is in line to results of prior studies, which found neutral stratification inside the SAL (Prospero and Carlson, 1972). Dropsonde measurements of Θ and r_m during NARVAL-II (Figure 4a) also indicate neutral stratification and a well-mixed SAL. At the top and at the bottom of the SAL radiative heating rates increase with altitude—an indicator of stable stratification, which is also marked by positive changes of Θ in dropsonde measurements. Those stable stratified regions mark the two bounding inversions that come along with SALs (Carlson & Prospero, 1972; Dunion & Velden, 2004; Ismail et al., 2010).

Mixing inside the SAL was found to be a possible explanation why large supermicron mineral dust particles are still found after long-range transport and are not removed from the SAL by gravitational settling processes during transport (Weinzierl et al., 2017). Gasteiger et al. (2017) used an integrated model to investigate particle settling during SAL advection and suggested that convective mixing within the SAL could explain the presence of supermicron particles at the other side of the Atlantic Ocean. However, performed calculations of the radiative effect near dust source regions without consideration of the actual water vapor profile could not explain the vertical mixing. Lidar measurements during NARVAL-II, however, indicated that Saharan dust transport is always accompanied by enhanced embedded SAL water vapor compared to the surrounding dry free troposphere. For the first time, it was shown that water vapor is a major contributor to the formation of the atmospheric heating rate profile inside the SAL. It is promoting vertical mixing inside the layer as well as sustaining the layers bounding inversions and could therefore counteract mineral dust settling processes from the SAL.

Acknowledgments
The data used in this publication were collected during the NARVAL-II (Next-generation Aircraft Remote-Sensing for Validation Studies-II) campaign and are made available through the DLR Institute for Atmospheric Physics in the HALO database (German Aerospace Center, 2016). The authors like to thank the staff members of the DLR HALO aircraft from DLR Flight Experiments for preparing and performing the measurement flights. Dakar radiosonde data were obtained from the freely accessible repository of the University of Wyoming (http://www.uwyo.edu/atsc). NARVAL-II was funded with the support of the Max Planck Society, the German Research Foundation (DFG Priority Program: HALO-SSP 1294) and the German Aerospace Center (DLR). This study was funded by a DLR VO-R young investigator group within the Institute of Atmospheric Physics.

References

Anderson, G. P., Clough, S. A., Kneizys, F. X., Chetwynd, J. H., & Shettle, E. P. (1986). AFGL atmospheric constituent profiles (0-120 km) (Tech. Rep.).

Bellouin, N., Boucher, O., Vesperini, M., & Tanré, D. (2004). Estimating the direct aerosol radiative perturbation: Impact of ocean surface representation and aerosol non-sphericity. *Quarterly Journal of the Royal Meteorological Society*, *130*(601), 2217–2232. https://doi.org/10.1256/qj.03.136

Boose, Y., Sierau, B., Garcia, M. I., Rodriguez, S., Alastuey, A., Linke, C., et al. (2016). Ice nucleating particles in the Saharan air layer. *Atmospheric Chemistry and Physics*, *16*(14), 9067–9087. https://doi.org/10.5194/acp-16-9067-2016

Buras, R., Dowling, T., & Emde, C. (2011). New secondary-scattering correction in DISORT with increased efficiency for forward scattering. *Journal of Quantitative Spectroscopy & Radiative Transfer*, *112*(12), 2028–2034. https://doi.org/10.1016/j.jqsrt.2011.03.019

Burton, S. P., Ferrare, R. A., Hostetler, C. A., Hair, J. W., Rogers, R. R., Obland, M. D., et al. (2012). Aerosol classification using airborne high spectral resolution lidar measurements—Methodology and examples. *Atmospheric Measurement Techniques*, *5*(1), 73–98. https://doi.org/10.5194/amt-5-73-2012

Carlson, T. N., & Prospero, J. M. (1972). The large-scale movement of Saharan air outbreaks over the northern equatorial Atlantic. *Journal of Applied Meteorology*, *11*(2), 283–297. https://doi.org/10.1175/1520-0450(1972)011<0283:TLSMOS>2.0.CO;2

Cox, C., & Munk, W. (1954). Measurement of the roughness of the sea surface from photographs of the Sun's glitter. *Journal of the Optical Society of America*, *44*(11), 838–850. https://doi.org/10.1364/JOSA.44.000838

d'Almeida, G. A., Koepke, P., & Shettle, E. P. (1991). *Atmospheric aerosols* (p. 561). Hampton, Virginia, USA: A. Deepak Publ.

Dunion, J. P., & Velden, C. S. (2004). The impact of the Saharan air layer on Atlantic tropical cyclone activity. *Bulletin of the American Meteorological Society*, *85*(3), 353–366. https://doi.org/10.1175/BAMS-85-3-353

Emde, C., Buras-Schnell, R., Kylling, A., Mayer, B., Gasteiger, J., Hamann, U., et al. (2016). The libRadtran software package for radiative transfer calculations (version 2.0.1). *Geoscientific Model Development*, *9*(5), 1647–1672. https://doi.org/10.5194/gmd-9-1647-2016

Esselborn, M., Wirth, M., Fix, A., Tesche, M., & Ehret, G. (2008). Airborne high spectral resolution lidar for measuring aerosol extinction and backscatter coefficients. *Applied Optics*, *47*(3), 346–358. https://doi.org/10.1364/AO.47.000346

Fu, Q., & Liou, K. N. (1992). On the correlated k-distribution method for radiative transfer in nonhomogeneous atmospheres. *Journal of the Atmospheric Sciences*, *49*(22), 2139–2156. https://doi.org/10.1175/1520-0469(1992)049<2139:otcdmf>2.0.co;2

Gasteiger, J., Groß, S., Sauer, D., Haarig, M., Ansmann, A., & Weinzierl, B. (2017). Particle settling and vertical mixing in the Saharan air layer as seen from an integrated model, lidar, and in situ perspective. *Atmospheric Chemistry and Physics*, *17*(1), 297–311. https://doi.org/10.5194/acp-17-297-2017

German Aerospace Center (2016). HALO database, avaiable at halo-db.pa.op.dlr.de, last access 13. *Aug*, *2019*.

Groß, S., Freudenthaler, V., Schepanski, K., Toledano, C., Schäfler, A., Ansmann, A., & Weinzierl, B. (2015). Optical properties of long-range transported Saharan dust over Barbados as measured by dual-wavelength depolarization Raman lidar measurements. *Atmospheric Chemistry and Physics*, *15*(19), 11,067–11,080. https://doi.org/10.5194/acp-15-11067-2015

Groß, S., Gasteiger, J., Freudenthaler, V., Müller, T., Sauer, D., Toledano, C., & Ansmann, A. (2016). Saharan dust contribution to the Caribbean summertime boundary layer – a lidar study during SALTRACE. *Atmospheric Chemistry and Physics*, *16*(18), 11,535–11,546. https://doi.org/10.5194/acp-16-11535-2016

Groß, S., Wiegner, M., Freudenthaler, V., & Toledano, C. (2011). Lidar ratio of Saharan dust over Cape Verde islands: Assessment and error calculation. *Journal of Geophysical Research*, *116*, D15203. https://doi.org/10.1029/2010JD015435

Huneeus, N., Schulz, M., Balkanski, Y., Griesfeller, J., Prospero, J., Kinne, S., et al. (2011). Global dust model intercomparison in AeroCom phase I. *Atmospheric Chemistry and Physics*, *11*(15), 7781–7816. https://doi.org/10.5194/acp-11-7781-2011

Ismail, S., Ferrare, R. A., Browell, E. V., Chen, G., Anderson, B., Kooi, S. A., et al. (2010). LASE measurements of water vapor, aerosol, and cloud distributions in Saharan air layers and tropical disturbances. *Journal of the Atmospheric Sciences*, *67*(4), 1026–1047. https://doi.org/10.1175/2009JAS3136.1

Jung, E., Albrecht, B., Prospero, J. M., Jonsson, H. H., & Kreidenweis, S. M. (2013). Vertical structure of aerosols, temperature, and moisture associated with an intense African dust event observed over the eastern Caribbean. *Journal of Geophysical Research-Atmospheres*, *118*, 4623–4643. https://doi.org/10.1002/jgrd.50352

Kanitz, T., Ansmann, A., Seifert, P., Engelmann, R., Kalisch, J., & Althausen, D. (2013). Radiative effect of aerosols above the northern and southern Atlantic Ocean as determined from shipborne lidar observations. *Journal of Geophysical Research; Atmospheres*, *118*, 12,556–12,565. https://doi.org/10.1002/2013jd019750

Kanitz, T., Engelmann, R., Heinold, B., Baars, H., Skupin, A., & Ansmann, A. (2014). Tracking the Saharan air layer with shipborne lidar across the tropical Aatlantic. *Geophysical Research Letters*, *41*, 1044–1050. https://doi.org/10.1002/2013gl058780

Karydis, V. A., Kumar, P., Barahona, D., Sokolik, I. N., & Nenes, A. (2011). On the effect of dust particles on global cloud condensation nuclei and cloud droplet number. *Journal of Geophysical Research*, *116*, D23204. https://doi.org/10.1029/2011jd016283

Kato, S., Ackerman, T. P., Mather, J. H., & Clothiaux, E. E. (1999). The k-distribution method and correlated-k approximation for a shortwave radiative transfer model. *Journal of Quantitative Spectroscopy & Radiative Transfer*, *62*(1), 109–121. https://doi.org/10.1016/s0022-4073(98)00075-2

Kiemle, C., Wirth, M., Fix, A., Ehret, G., Schumann, U., Gardiner, T., et al. (2008). First airborne water vapor lidar measurements in the tropical upper troposphere and mid-latitudes lower stratosphere: accuracy evaluation and intercomparisons with other instruments. *Atmospheric Chemistry and Physics*, *8*(17), 5245–5261. https://doi.org/10.5194/acp-8-5245-2008

Kinne, S., Schulz, M., Textor, C., Guibert, S., Balkanski, Y., Bauer, S. E., et al. (2006). An AeroCom initial assessment—Optical properties in aerosol component modules of global models. *Atmospheric Chemistry and Physics*, *6*(7), 1815–1834. https://doi.org/10.5194/acp-6-1815-2006

Koepke, P., Gasteiger, J., & Hess, M. (2015). Technical note: Optical properties of desert aerosol with non-spherical mineral particles: data incorporated to OPAC. *Atmospheric Chemistry and Physics*, *15*(10), 5947–5956. https://doi.org/10.5194/acp-15-5947-2015

Krautstrunk, M., & Giez, A. (2012). The transition from FALCON to HALO era airborne atmospheric research. In U. Schumann (Ed.), *Atmospheric Physics* (pp. 609–624). Berlin, Heidelberg: Springer.

Li, F., Vogelmann, A. M., & Ramanathan, V. (2004). Saharan dust aerosol radiative forcing measured from space. *Journal of Climate*, *17*(13), 2558–2571. https://doi.org/10.1175/1520-0442(2004)017<2558:sdarfm>2.0.co;2

Lilly, D. K. (1968). Models of cloud-topped mixed layers under a strong inversion. *Quarterly Journal of the Royal Meteorological Society*, *94*(401), 292–309. https://doi.org/10.1002/qj.49709440106

Mallet, M., Tulet, P., Serça, D., Solmon, F., Dubovik, O., Pelon, J., et al. (2009). Impact of dust aerosols on the radiative budget, surface heat fluxes, heating rate profiles and convective activity over West Africa during March 2006. *Atmospheric Chemistry and Physics*, *9*(18), 7143–7160. https://doi.org/10.5194/acp-9-7143-2009

Mamouri, R.-E., & Ansmann, A. (2016). Potential of polarization lidar to provide profiles of CCN- and INP-relevant aerosol parameters. *Atmospheric Chemistry and Physics*, *16*(9), 5905–5931. https://doi.org/10.5194/acp-16-5905-2016

Marsham, J. H., Parker, D. J., Grams, C. M., Johnson, B. T., Grey, W. M. F., & Ross, A. N. (2008). Observations of mesoscale and boundary-layer scale circulations affecting dust transport and uplift over the Sahara. *Atmospheric Chemistry and Physics*, *8*(23), 6979–6993. https://doi.org/10.5194/acp-8-6979-2008

Mayer, B., & Kylling, A. (2005). Technical note: The libRadtran software package for radiative transfer calculations—Description and examples of use. *Atmospheric Chemistry and Physics*, *5*(7), 1855–1877. https://doi.org/10.5194/acp-5-1855-2005

Moulin, C., Lambert, C. E., Dulac, F., & Dayan, U. (1997). Control of atmospheric export of dust from North Africa by the North Atlantic oscillation. *Nature*, *387*(6634), 691–694. https://doi.org/10.1038/42679

Prospero, J. M., & Carlson, T. N. (1972). Vertical and areal distribution of Saharan dust over the western equatorial North Atlantic Ocean. *Journal of Geophysical Research*, *77*(27), 5255–5265. https://doi.org/10.1029/JC077i027p05255

Satheesh, S., & Moorthy, K. K. (2005). Radiative effects of natural aerosols: A review. *Atmospheric Environment*, *39*(11), 2089–2110. https://doi.org/10.1016/j.atmosenv.2004.12.029

Stamnes, K., Tsay, S.-C., Wiscombe, W., & Jayaweera, K. (1988). Numerically stable algorithm for discrete-ordinate-method radiative transfer in multiple scattering and emitting layered media. *Applied Optics*, *27*(12), 2502. https://doi.org/10.1364/ao.27.002502

Stein, A. F., Draxler, R. R., Rolph, G. D., Stunder, B. J. B., Cohen, M. D., & Ngan, F. (2015). NOAA's HYSPLIT atmospheric transport and dispersion modeling system. *Bulletin of the American Meteorological Society*, *96*(12), 2059–2077. https://doi.org/10.1175/BAMS-D-14-00110.1

Stevens, B., Ament, F., Bony, S., Crewell, S., Ewald, F., Groß, S., et al. (2019). A high-altitude long-range aircraft configured as a cloud observatory: The NARVAL expeditions. *Bulletin of the American Meteorological Society*, *100*(6), 1061–1077. https://doi.org/10.1175/BAMS-D-18-0198.1

Tesche, M., Ansmann, A., Müller, D., Althausen, D., Engelmann, R., Freudenthaler, V., & Groß, S. (2009). Vertically resolved separation of dust and smoke over Cape Verde using multiwavelength raman and polarization lidars during Saharan Mineral Dust Experiment 2008. *Journal of Geophysical Research*, *114*, D13202. https://doi.org/10.1029/2009jd011862

Waterman, P. C. (1971). Symmetry, unitarity, and geometry in electromagnetic scattering. *Physical Review D*, *3*, 825–839. https://doi.org/10.1103/PhysRevD.3.825

Weinzierl, B., Ansmann, A., Prospero, J. M., Althausen, D., Benker, N., Chouza, F., et al. (2017). The Saharan Aerosol Long-Range Transport and Aerosol-Cloud-interaction Experiment: Overview and selected highlights. *Bulletin of the American Meteorological Society*, *98*(7), 1427–1451. https://doi.org/10.1175/BAMS-D-15-00142.1

Wirth, M., Fix, A., Mahnke, P., Schwarzer, H., Schrandt, F., & Ehret, G. (2009). The airborne multi-wavelength water vapor differential absorption lidar WALES: System design and performance. *Applied Physics B: Lasers and Optics*, *96*(1), 201–213. https://doi.org/10.1007/s00340-009-3365-7

Wong, S., Dessler, A. E., Mahowald, N. M., Yang, P., & Feng, Q. (2009). Maintenance of lower tropospheric temperature inversion in the Saharan air layer by dust and dry anomaly. *Journal of Climate*, *22*(19), 5149–5162. https://doi.org/10.1175/2009jcli2847.1

Zhu, A., Ramanathan, V., Li, F., & Kim, D. (2007). Dust plumes over the Pacific, Indian, and Atlantic oceans: Climatology and radiative impact. *Journal of Geophysical Research*, *112*, D16208. https://doi.org/10.1029/2007jd008427